Article

Synergy of single atoms and sulfur vacancies for advanced polysulfide–iodide redox flow battery

Zhigui Wang[1,2,7], Guolong Lu[1,2,7], Tianran Wei[2,3], Ge Meng [1] ✉, Haoxiang Cai[2], Yanhong Feng[2], Ke Chu [3] ✉, Jun Luo [4], Guangzhi Hu [5], Dingsheng Wang [6] ✉ & Xijun Liu [2] ✉

Aqueous redox flow batteries (RFBs) incorporating polysulfide/iodide chemistries have received considerable attention due to their safety, high scalability, and cost-effectiveness. However, the sluggish redox kinetics restricted their output energy efficiency and power density. Here we designed a defective MoS_2 nanosheets supported Co single-atom catalyst that accelerated the transformation of S^{2-}/S_x^{2-} and I^-/I_3^- redox couples, hence endow the derived polysulfide–iodide RFB with an initial energy efficiency (EE) of 87.9% and an overpotential of 113 mV with an average EE 80.4% at 20 mA cm^{-2} and 50% state-of-charge for 50 cycles, and a maximal power density of 95.7 mW cm^{-2} for an extended cycling life exceeding 850 cycles at 10 mA cm^{-2} and 10% state-of-charge. In situ experimental and theoretical analyses elucidate that Co single atoms induce the generation of abundant sulfur vacancies in MoS_2 via a phase transition process, which synergistically contributed to the enhanced adsorption of reactants and key reaction intermediates and improved charge transfer, resulting in the enhanced RFB performance.

The global challenge of energy crises underscores the importance of addressing the massive depletion of fossil fuels. In this case, aqueous redox flow batteries (RFBs) have received great attention due to their high scalability, design flexibility, capability to decouple power and energy, and enhanced safety, showing an excellent suitability for grid integration to alleviate the intermittent and fluctuating nature inherent in renewable energy sources[1,2]. Notably, the sulfide/polysulfide (S^{2-}/S_x^{2-}) and iodide/triiodide (I^-/I_3^-) redox couples exhibit high solubility and cost-effectiveness[3,4]; and thus, the polysulfide/iodide–based RFBs (SIRFBs) become an appealing candidate[5–7]. However, the multistep charge transfer reactions within the S^{2-}/S_x^{2-} and I^-/I_3^- couples on

electrode result in elevated polarization resistance and poor kinetic reversibility[8,9], which induce slow adsorption behavior, limited operational lifespan, and diminished energy efficiency (EE), thereby impeding the widespread adoption of SIRFBs[10,11]. Therefore, designing efficient and stable catalytic electrodes to accelerate the transformation of S^{2-}/S_x^{2-} and I^-/I_3^- couples remains challenging but crucial for practical deployment of SIRFBs.

Many metal sulfides[12–18], such as CoS_2, $CoS_2@CoS$, Cu_7S_4, $NiCo_2S_4$, and $CuFeS_2$, had shown substantial potential applications in SIRFBs to boost the S^{2-}/S_x^{2-} and I^-/I_3^- redox couples with suppressed side reactions. Recently, the two-dimensional molybdenum disulfide (MoS_2) has

[1]Key Laboratory of Carbon Materials of Zhejiang Province, College of Chemistry and Materials Engineering, Wenzhou University, Wenzhou 325035, China. [2]Guangxi Key Laboratory of Processing for Non-ferrous Metals and Featured Materials, School of Chemistry and Chemical Engineering, Guangxi University, Nanning 530004 Guangxi, China. [3]School of Materials Science and Engineering, Lanzhou Jiaotong University, Lanzhou 730070, China. [4]ShenSi Lab, Shenzhen Institute for Advanced Study, University of Electronic Science and Technology of China, Longhua District, Shenzhen 518110, China. [5]School of Ecology and Environmental Science, Yunnan University, Kunming 650504, China. [6]Department of Chemistry, Tsinghua University, 100084 Beijing, China. [7]These authors contributed equally: Zhigui Wang, Guolong Lu. ✉e-mail: mengge@wzu.edu.cn; chukelut@163.com; wangdingsheng@mail.tsinghua.edu.cn; xjliu@gxu.edu.cn
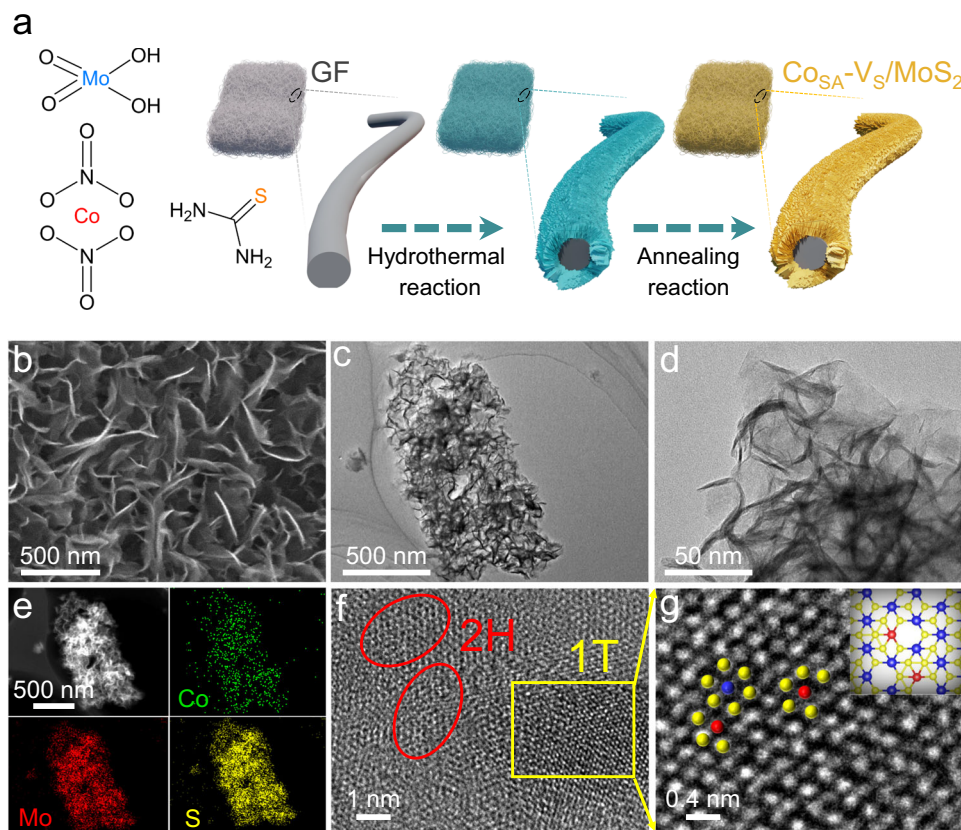
Fig. 1 | Microstructural characterizations of the Co_{SA}-V_S/MoS_2 nanosheets. a Scheme diagram for the Co_{SA}-V_S/MoS_2 synthetic process. **b** SEM, **c** TEM, **d** STEM, **e** EDX, **f**, **g** AC-HAADF-STEM images of Co_{SA}-V_S/MoS_2 (yellow sphere: S atom, red sphere: Co atom, blue sphere: Mo atom).

received considerable attention in electrocatalysis and battery fields because of its unique electronic structures and defective properties[19–21]. Particularly, MoS_2 was able to improve the polysulfide shuttle process for Li–S batteries[22] and accelerate the I^-/I_3^- redox reaction in Zn−I_2 RFBs[23], respectively; while its application in SIRFB has not been reported yet. Meanwhile, the intrinsic activity of MoS_2 still needs to be further improved to meet the high-power demand of industrial RFBs. In recent years, single atom catalysts (SACs) have attracted widespread attention in heterogeneous catalysis and electrocatalysis fields due to the merits of maximal atom utilization, low-coordination environment, and abundant unoccupied orbitals, etc.[24–26]. This concept provides new opportunities for exploring high-performance electrocatalysts for RFBs. The single atoms anchoring onto MoS_2 surface can not only introduce new-type and highly active catalytic sites, but also regulate the defective structure and electronic property of MoS_2 substrate, which will synergistically optimize the comprehensive performance of SIRFBs. However, the application of SA-doped MoS_2 in SIRFBs has not yet been reported, presenting an opportunity to contribute novel insights and address existing gaps in the research field.

Given the above-mentioned considerations, a reasonable design and application of Co SA doped S vacancies-containing MoS_2 (Co_{SA}-V_S/MoS_2) in the SIRFB is firstly proposed. The derived SIRFB achieved an EE of 87.9% at 20 mA cm^{-2}, which is higher than that of the reported CoS_2/CoS (71.6%)[12], Cu_2CoGeS_4 (77.2%)[13], Cu_7S_4 (78.5%)[14], $CuFeS_2$ (79.6%)[18], etc. Besides, the battery exhibited a peak power density of 95.7 mW cm^{-2} and an average EE of 76.5% at 30 mA cm^{-2} within 50 cycles, greater than those of the reported Cu_7S_4/CNT (84.6 mW cm^{-2}, 66%)[16] and $NiCo_2S_4$@CP (82.4 mW cm^{-2}, 72.4%)[17] catalysts. It also demonstrated a cycling life of approximately 850 cycles during continuous operation at 10 mA cm^{-2} with a 10% state of charge (SOC) and a low overpotential of 113 mV at 20 mA cm^{-2}. Signally, the initial EE of 93.1% could be almost fully

recovered after refreshing the electrolytes (200th and 600th cycles). And, more details can be found in Supplementary Table 1. Those suggest the advantage of the designed SIRFB with Co_{SA}-V_S/MoS_2. The in situ Raman and in situ UV–vis experiments, catalytic tests, and density functional theory (DFT) calculations reveal that the introduction of Co_{SA} to MoS_2 stimulated a phase transformation from trigonal prismatic to metallic octahedral and triggered the formation of vacancy defects. Consequently, Co_{SA} and Vs sites synergistically optimized the interface electronic structure, promoted the reactant adsorption capacity, and accelerated the kinetics of S^{2-}/S_x^{2-} and I^-/I_3^- redox couples, simultaneously.

Results

Synthesis and characterization

The Co_{SA}-V_S/MoS_2 hybrids on graphite felt (GF) were synthesized using a one-step solvothermal in situ growth strategy, following the annealing activation process, as illustrated in Fig. 1a, with detailed information provided in "Methods" section. The scanning electron microscopy (SEM) images of GF, MoS_2, and Co_{SA}-V_S/MoS_2 are depicted in Supplementary Fig. 1 and Fig. 1b, revealing the uniform distribution of nanosheet-like arrays with a lateral size of approximately 350 to 450 nm on the pristine GF surface, which endows fast charge transport and robust mechanical stability. Of note, the introduction of Co_{SA} did not change the morphology of MoS_2. Meantime, these nanosheets are interconnected to each other thus forming a porous structure, leading to more active edge sites exposed and effective mass transportability. Further morphological analyses using transmission electron microscopy (TEM), scanning transmission electron microscopy (STEM) and energy-dispersive X-ray spectroscopy (EDX) mapping are presented in Fig. 1c–e, demonstrating a nanosheet-like architecture with Co, Mo, and S evenly distributed, which corroborates well with the SEM results.
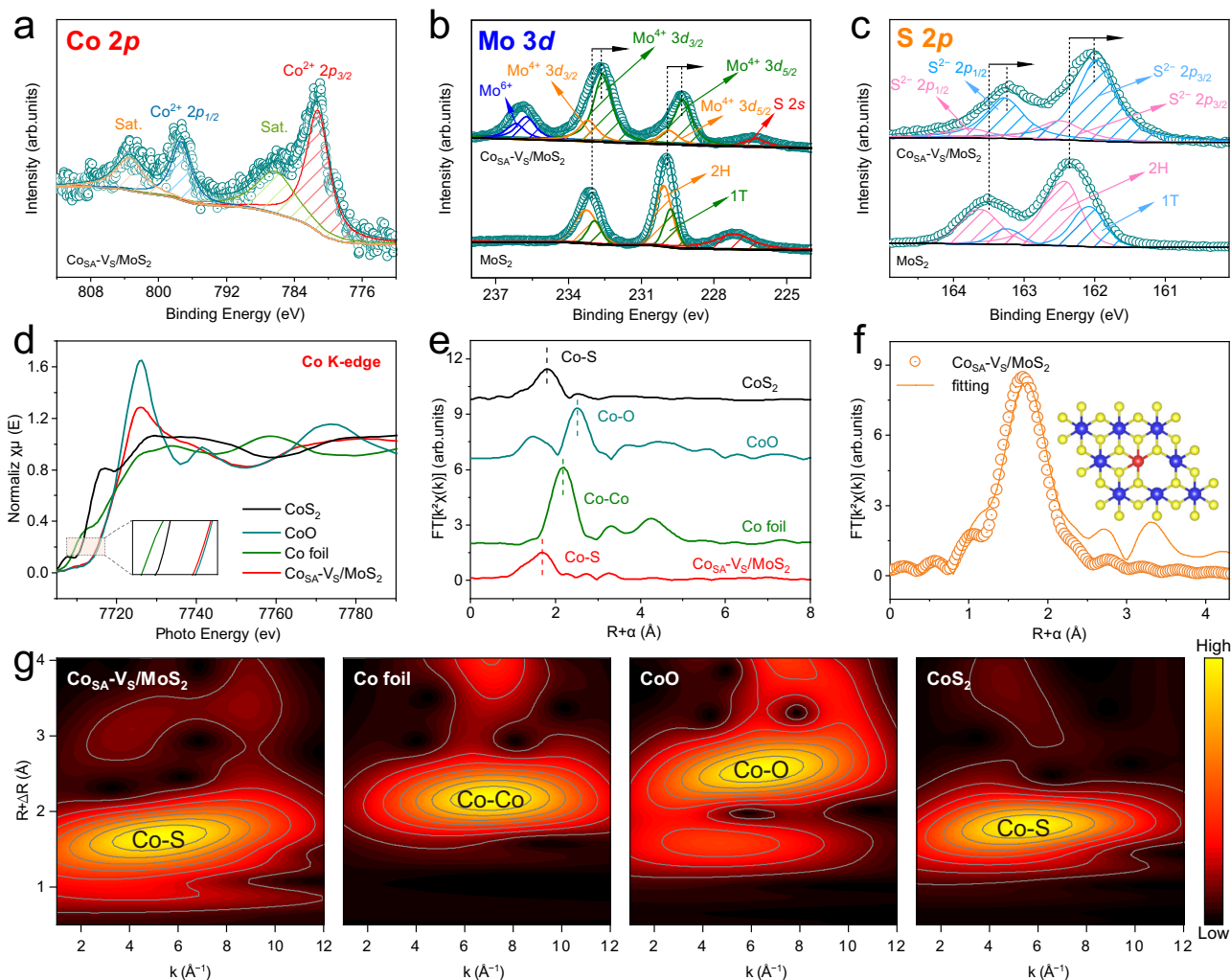
Fig. 2 | Analysis of XPS and XAFS spectra. a Co 2*p* XPS spectra of Co$_{SA}$-V$_S$/MoS$_2$. **b**, **c** Mo 3*d* and S 2*p* XPS spectra of Co$_{SA}$-V$_S$/MoS$_2$ and MoS$_2$. **d**, **e** XANES spectra extracted from the Co K-edge and the corresponding FT-EXAFS at the *R* space of Co$_{SA}$-V$_S$/MoS$_2$ and the reference samples. **f** FT-EXAFS fitting curve at the *R* space of Co$_{SA}$-V$_S$/MoS$_2$ at the Co K-edge (yellow sphere: S atom, red sphere: Co atom, blue sphere: Mo atom). **g** Wavelet transform contour plots of Co$_{SA}$-V$_S$/MoS$_2$ and the reference samples.

X-ray powder diffraction (XRD) measurements and Raman characterizations were simultaneously conducted on GF, MoS$_2$, and Co$_{SA}$-V$_S$/MoS$_2$, and the results are presented in Supplementary Fig. 2. Clearly, MoS$_2$ and Co$_{SA}$-V$_S$/MoS$_2$ display characteristic diffraction peaks at 14.4° and 35.8°, corresponding to the (002) and (102) planes of pristine MoS$_2$ (PDF#37-1492)[27], respectively (Supplementary Fig. 2a and Supplementary Note 1). The weakened (002) peak in Co$_{SA}$-V$_S$/MoS$_2$ is attributed to the defect enrichment arise from the introduction of Co atoms[28,29]. Additionally, the Raman spectra reveal the characteristic MoS$_2$ peaks of E$_{2g}^1$ (379 cm^{-1}) and A$_{1g}$ (407 cm^{-1}) in Co$_{SA}$-V$_S$/MoS$_2$ (Supplementary Fig. 2b). High-resolution TEM (HRTEM) analysis of Co$_{SA}$-V$_S$/MoS$_2$ (Supplementary Fig. 2c) indicates the (002) plane of 2H-MoS$_2$ (PDF#37-1492) with a lattice spacing of 0.616 nm, conforming the XRD result. Moreover, the spherical aberration-corrected high-angle annular dark-field STEM (AC-HAADF-STEM) is decidedly showed the detailed interfacial with hexagonal lattice structure in the synthesized Co$_{SA}$-V$_S$/MoS$_2$, and the metallic octahedral 1T-MoS$_2$ appears after Co SA-doping (Fig. 1f, g). This implies that the introduction of Co contributes the arrangement of S atoms and facilitates the phase formation of 1T-MoS$_2$[30], resulting in the creation of abundant V$_S$ to boost the reaction intermediate of S^{2-}/S$_x^{2-}$ and I$^-$/I$_3^-$ redox couples adsorbing on adjacent S sites, which will be further verified by theoretical analyses. Furthermore, as can be seen from

Supplementary Fig. 3, the marked dark spots in MoS$_2$ lattice represent the single Co atoms, as evidenced by the corresponding cross-sectional intensity spectra.

The X-ray photoelectron spectroscopy (XPS) and X-ray absorption fine structure (XAFS) results of Co$_{SA}$-V$_S$/MoS$_2$ are presented in Fig. 2, which aim to further scrutinize its chemical compositions and bonding states. XPS provides direct evidence of the phase conversion from 2H to 1T after the introduction of Co atoms[31]. Supplementary Fig. 4a indicates the signals of Co, S, and Mo in the Co$_{SA}$-V$_S$/MoS$_2$, which agrees well with EDX mapping. In addition, the signal of Co was absent in MoS$_2$ (Supplementary Fig. 4b). The atomic ratio of Mo and Co species in the Co$_{SA}$-V$_S$/MoS$_2$ is determined to be approximately 34:1 (Supplementary Table 2). The Co 2*p* spectrum is deconvoluted into two peaks corresponding to Co^{2+} 2*p*$_{3/2}$ (781.3 eV) and Co^{2+} 2*p*$_{1/2}$ (797.4 eV), and two satellite peaks at 786.7 and 803.6 eV (Fig. 2a)[32]. In the Mo 3*d* XPS spectrum of Co$_{SA}$-V$_S$/MoS$_2$ (Fig. 2b), two distinctive characteristic peaks at 229.9 and 233.2 eV correspond to Mo 3*d*$_{5/2}$ and Mo 3*d*$_{3/2}$, respectively, indicating the presence of Mo^{4+} (2H-MoS$_2$)[33]. Concurrently, two predominant peaks at 229.3 and 232.6 eV can be indexed to the Mo^{4+} (1T-MoS$_2$)[33]. In addition, two peaks at 234 and 236 eV are assigned to Mo^{6+}, indicative of the formation of V$_S$[34]; and a peak at 226.6 eV originates from the S 2*s* signal[27,35]. Compared to MoS$_2$, a notable negative shift is observed in the Co$_{SA}$-V$_S$/MoS$_2$, further

verifying the generation of 1T-MoS_2 by SA-doping[31,36]. Importantly, this can be further explained by theoretical calculations (Supplementary Figs. 5 and 6). Regarding the S $2p$ spectrum of Co_{SA}-V_S/MoS_2 (Fig. 2c), two peaks at 162.0 and 163.1 eV are assigned to S $2p_{3/2}$ and S $2p_{1/2}$ of 1T MoS_2[37], respectively. Besides, two peaks at 162.5 and 163.8 eV, which are assigned to S $2p_{3/2}$ and S $2p_{1/2}$, respectively, represent 2H-MoS_2[37]. Similar negative shift in S $2p$ spectrum of the Co_{SA}-V_S/MoS_2 are attributed to the introduction of Co atoms, which triggers the formation of V_S and the lattice distortion, and thus evokes changes in bond energy[27]. Overall, the anchoring of Co atoms can effectively regulate the atom arrangement of MoS_2, thereby resulting in V_S and phase transformation, which is in accordance with AC-HAADF-STEM and XRD analyses.

XAFS analyses were further conducted to obtain deeper insights into the electronic structure and coordination characteristics of Co species in Co_{SA}-V_S/MoS_2. Figure 2d illustrates the Co K-edge X-ray absorption near-edge structure (XANES) spectrum of Co_{SA}-V_S/MoS_2, along with the reference spectra of CoS_2, CoO, and Co foil. The absorption edge of Co_{SA}-V_S/MoS_2 approaches to that of CoO, indicative of positive charged Co atoms with an average valence state approximately +2, consistent with the XPS results[38–40]. Coordination environment of Co atoms in Co_{SA}-V_S/MoS_2 is further elucidated through Fourier-transformed k-weighted extended X-ray absorption fine structure (FT-EXAFS) spectra (Fig. 2e), where the prominent peak at 1.70 Å can be attributed to the Co-S bond, slightly lower than that of CoS_2 (1.81 Å). This is due to the existence of V_S around Co_{SA} in Co_{SA}-V_S/MoS_2[41], which is evidenced by the fitting results (Fig. 2f). Clearly, no characteristic Co-Co bond is observed in Co_{SA}-V_S/MoS_2 (Fig. 2e), confirming that Co atoms are isolated dispersed. In addition, quantitative fitting results also identify that the Co_{SA} is coordinated to approximately five S atoms, while one S atom loss thus forming the V_S (Fig. 2f and Supplementary Table 3), which is in accordance with the previous report[41] and XPS analyses. Meanwhile, the wavelet transform contour plot of Co_{SA}-V_S/MoS_2 reveals a maximum intensity at -1.70 Å (Fig. 2g), corresponding to Co-S, further conforms the FT-EXAFS results[38,42]. These findings provide compelling evidence of the isolated dispersion of Co atoms and the formation of V_S in Co_{SA}-V_S/MoS_2.

Adsorption and electrocatalytic activity

The adsorption behavior of S_x^{2-} and I_3^- redox species plays a pivotal role in the electrocatalytic process (Supplementary Note 2). In this case, the combination of Co SA and V_S can optimize the electronic structure of Co_{SA}-V_S/MoS_2, and thereby promoting the adsorption and conversion kinetics of reactants and key intermediates[31,34,43,44]. Accordingly, the ultraviolet-visible (UV–vis) absorption spectra and calibration curve between absorption and solution concentration of S_x^{2-} and I_3^- with embedding GF, MoS_2, and Co_{SA}-V_S/MoS_2 electrode are shown in Fig. 3a, b, and the analyses were determined in the H-type cell with static diffusion tests via monitored the electrolyte side after 12 h (Fig. 3c, d). Compared to GF and MoS_2, Co_{SA}-V_S/MoS_2 exhibits more pronounced adsorption capacity toward I_3^- (Fig. 3a and Supplementary Table 4). This is further validated by the UV–vis absorption spectra where Co_{SA}-V_S/MoS_2 shows a significant weaker peak intensity at 290 and 352 nm associated with I_3^- ions in comparison with the counterparts, in line with calibration curve between absorption intensity and solution concentration (Fig. 3a). Similarly, Co_{SA}-V_S/MoS_2 displays a higher absorptivity for S^{2-} (260 nm), S_2^{2-} (310 nm) and S_4^{2-}/S_2^{2-} (370 nm) anions than that of GF and MoS_2 (Fig. 3b)[4,5], further affirmed by the recorded UV–vis spectra. Besides, the adsorption and permeability phenomena of I_3^- and S_x^{2-} redox species are intuitively observed in the H-type cells with static diffusion tests (Fig. 3c, d), respectively, which utilized the Nafion membranes (SEN-G115 and SEN-K117) to separate the deionized water chamber (colorless) and electrolyte chamber (yellow). Clearly, the Co_{SA}-V_S/MoS_2 and MoS_2 electrode in the I_3^- electrolyte have stronger adsorption capacity and restraint for I_3^-

shuttle than GF after 12 h resting, while in the S_x^{2-} electrolyte after resting for 12 h, Co_{SA}-V_S/MoS_2 electrode exhibits relatively better adsorption capacity for S_x^{2-} redox species than those of MoS_2 and GF.

Then, the electrocatalytic activities of Co_{SA}-V_S/MoS_2 toward S^{2-}/S_x^{2-} and I^-/I_3^- redox reactions were investigated by cyclic voltammetry (CV) measurements. The pair of peaks corresponding to the redox reactions of I^-/I_3^- couples exhibit a peak-to-peak separation (E_{pp}) of 0.24 V (Fig. 3e and Supplementary Table 5), lower than those of MoS_2 (0.29 V) and GF (0.32 V). This suggests that Co_{SA}-V_S/MoS_2 owns a higher activity towards the I^-/I_3^- conversion as compared to MoS_2 and GF. Meanwhile, Co_{SA}-V_S/MoS_2 possesses a larger peak current density compared to GF and MoS_2 (Fig. 3e)[45]. This further signifies that Co_{SA}-V_S/MoS_2 is active for the redox reaction of I^-/I_3^-. Furthermore, the J_{Ox}/$|J_{Red}|$ ratio of 0.68 for Co_{SA}-V_S/MoS_2 indicates its better reversibility to I^-/I_3^- redox reaction than those of MoS_2 (0.61) and GF (0.63). Besides, Co_{SA}-V_S/MoS_2 significantly enhances the electrochemical reactivity of the polysulfide couple with prominent redox peaks (Fig. 3f). The three reduction peaks imply that polysulfide may be transformed to S_x^{2-} ($x = 2-8$) species on Co_{SA}-V_S/MoS_2[46,47]. In addition, the Nyquist plots indicate that Co_{SA}-V_S/MoS_2 possesses an improved S^{2-}/S_x^{2-} conversion kinetics (Supplementary Fig. 7, Supplementary Table 6 and Supplementary Note 3). The above findings reveal that Co_{SA}-V_S/MoS_2 can effectively catalyze the transformation of S^{2-}/S_x^{2-} and I^-/I_3^- couples. Besides, the diffusion-controlled S^{2-}/S_x^{2-} and I^-/I_3^- redox reaction processes on Co_{SA}-V_S/MoS_2 surface were evidenced by their linear relationship between the peak currents and the square root of the scan rate ($v^{1/2}$, Supplementary Figs. 8 and 9). Additionally, according to the Berzins−Delahay equation, the order of the calculated I^- diffusion coefficient (D) follows: GF < MoS_2 < Co_{SA}-V_S/MoS_2, in accordance with the battery performances. Furthermore, Co_{SA}-V_S/MoS_2 presents stable activities toward I^-/I_3^- and S^{2-}/S_x^{2-} redox reactions over 100 cycles (Supplementary Fig. 10).

The reaction mechanism of S^{2-}/S_x^{2-} and I^-/I_3^- conversion was further monitored by in situ UV−vis experiments (Supplementary Figs. 11 and 12). The characteristic peaks corresponding S_4^{2-}/S_2^{2-} (362 nm) and S_2^{2-} (331 nm) are detected (Supplementary Fig. 12a), evidencing that the occurrence of $S^{2-} \leftrightarrow S_x^{2-}$ conversion[4]. Of note, the intensity of S_4^{2-}/S_2^{2-} and S_4^{2-} reduces during the oxidation process and increases at the reduction reaction (Supplementary Fig. 12b). Similarly, the characteristic peaks of I_3^- (288 and 354 nm) are observed (Supplementary Fig. 12c), indicating the polyiodides response in the electrolyte for $I^- \leftrightarrow I_3^-$ conversion[48,49]; while the intensity of I_3^- increases during the oxidation process and reduces at the reduction reaction (Supplementary Fig. 12d).

Density functional theory (DFT) calculations

To reveal the catalytic enhancement of Co_{SA}-V_S/MoS_2, DFT simulations were performed (Supplementary Note 4). The total density of states (DOS) of two models evidence that Co_{SA} and V_S collectively induce spin polarization states (Fig. 4a)[50], resulting in higher conductivity and affinity toward intermediates compared with MoS_2[51–53]. This guarantees a fast charge transfer of redox reactions, accounting for enhanced catalytic activity of Co_{SA}-V_S/MoS_2[54,55]. Further, Co_{SA}-V_S/MoS_2 has lower adsorption energy toward I^-, I_2, I_3^-, S^{2-}, S_2^{2-}, S_4^{2-}, S_6^{2-}, and S_8^{2-} intermediates as compared to those of MoS_2 (Fig. 4b, Supplementary Fig. 13 and Supplementary Data 1), demonstrating that Co_{SA}-V_S/MoS_2 present a higher affinity to those reaction intermediates (Supplementary Table 7), which is in line with the adsorption behaviors and UV−vis analyses (Fig. 3a, b).

The transformation of I^-/I_3^- can be divided into four steps, while the S^{2-}/S_x^{2-} couple includes six steps, as illustrated in Fig. 4c, Supplementary Fig. 14 and Supplementary Data 1; where the elementary reaction of $* \to *I^-$, $*I_2 \to *I_3^-$, and $*S^{2-} \to *S_2^{2-}$ are the corresponding potential-determining steps (PDSs). Clearly, Co_{SA}-V_S/MoS_2 shows PDS energy barrier of 0.14 eV in the elementary reaction of $* \to *I^-$ (Fig. 4d), significantly lower than MoS_2 (0.54 eV) in the elementary reaction of $*I_2 \to *I_3^-$,
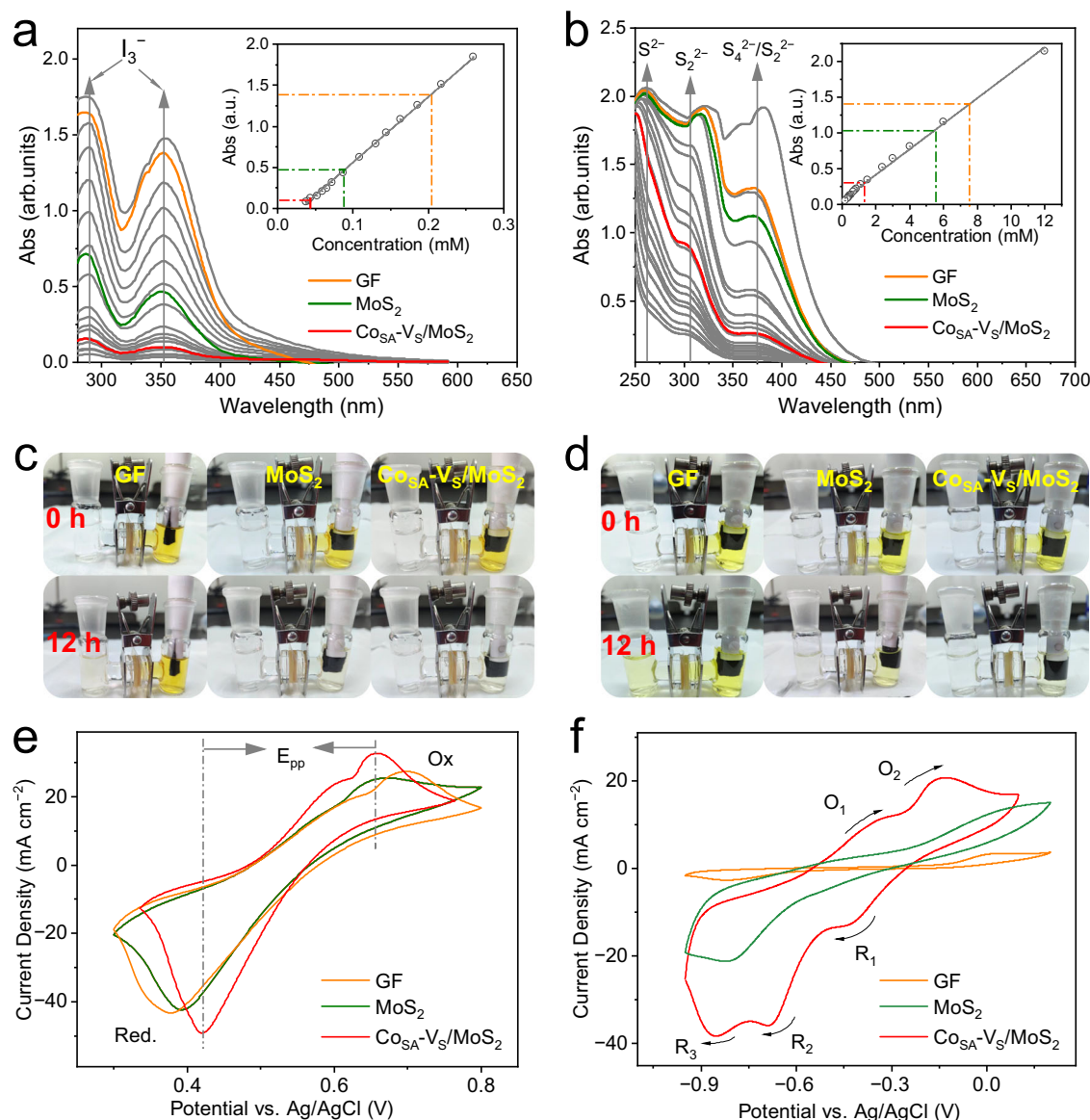
Fig. 3 | Adsorption and cyclic voltammetry characterizations. a, b UV–vis spectra of the I_3^- and S_2^{2-} solutions with GF, MoS_2, and Co_{SA}-V_S/MoS_2 impregnation for 12 h, and the inset is the calibration curve between absorption intensity and concentration (at $25 \pm 2\,°C$, in the environmental atmosphere). **c, d** Digital images of I_3^- and S_x^{2-} diffusion and adsorption behavior in I_3^- and S_2^{2-} solution with GF,

MoS_2, and Co_{SA}-V_S/MoS_2 impregnation for 12 h (left chamber: deionized water; right chamber: 5.2 mM NaI + 1.3 mM I_2 or 12 mM Na_2S_2). **e, f** CV curves of the catalysts recorded in 0.1 M NaI_3 + 0.5 M NaCl solution and 0.06 M Na_2S + 0.02 M S + 0.5 M NaCl solution, respectively, at a scan rate of 50 mV s^{-1}.

implying an energy-favorable process. Interestingly, it is found that the PDS energy barrier corresponds to S^{2-}/S_x^{2-} on Co_{SA}-V_S/MoS_2 is 0.38 eV (Fig. 4e), smaller than that on MoS_2 (0.68 eV), leading to the high performance of Co_{SA}-V_S/MoS_2 towards polysulfide species transformation (Fig. 4c). Similarly, the DFT calculation of Co doped in MoS_2 without V_S (Co_{SA}/MoS_2) and pristine V_S in MoS_2 (V_S/MoS_2) models also have been implemented (Supplementary Fig. 15), the corresponding PDSs energy barrier of I^-/I_3^- (0.34 eV) and S^{2-}/S_x^{2-} (0.48 eV) redox in Co_{SA}/MoS_2, and the PDSs energy barrier of I^-/I_3^- (0.46 eV) and S^{2-}/S_x^{2-} (0.45 eV) redox in V_S/MoS_2 are all higher than those of Co_{SA}-V_S/MoS_2 and below the MoS_2. Therefore, both experimental results and DFT simulations confirm that Co_{SA} sites effectively promote the activity of I^-/I_3^- and S^{2-}/S_x^{2-} redox, and thus favors the SIRFB performance.

Redox flow battery performance

A schematic representation of the proposed SIRFB configuration is depicted in Fig. 5a. SIRFB with Co_{SA}-V_S/MoS_2 as anodic and cathodic

catalyst was assembled, and the 2.0 M Na_2S_2 and 2.0 M NaI + 0.5 M I_2 were adopted as anolyte and catholyte, respectively (Supplementary Fig. 16). A two-layer separator consisting of G115 and K117 was used to enhance Na^+ cation transport and restrict the crossover of active species[56]. Electrochemical impedance spectroscopy (EIS) spectra indicate that the charge transfer resistance (R_{ct}) on Co_{SA}-V_S/MoS_2 is $0.76\,\Omega\,cm^{-2}$ (Fig. 5b and Supplementary Fig. 17), smaller than that on GF ($18.81\,\Omega\,cm^{-2}$) and MoS_2 ($0.85\,\Omega\,cm^{-2}$). Of note, the solution resistance (R_s) on Co_{SA}-V_S/MoS_2 is $3.42\,\Omega\,cm^{-2}$ (Supplementary Table 8), lower than those on GF ($4.67\,\Omega\,cm^{-2}$) and MoS_2 ($3.88\,\Omega\,cm^{-2}$). These results evidence that Co_{SA}-V_S/MoS_2 is capable of facilitating charge transfer and promoting diffusion dynamics[12], which is consistent with the CV experiments and DOS analyses. Figure 5c and Supplementary Fig. 18 depict the first charge and discharge curves of SIRFBs recorded at 15 mA cm^{-2} associated with 100% SOC. Evidently, the SIRFB with Co_{SA}-V_S/MoS_2 exhibits the highest capacity of 131.2 mAh, surpassing those of MoS_2 (117 mAh) and GF (93.1 mAh). Besides, the first charge
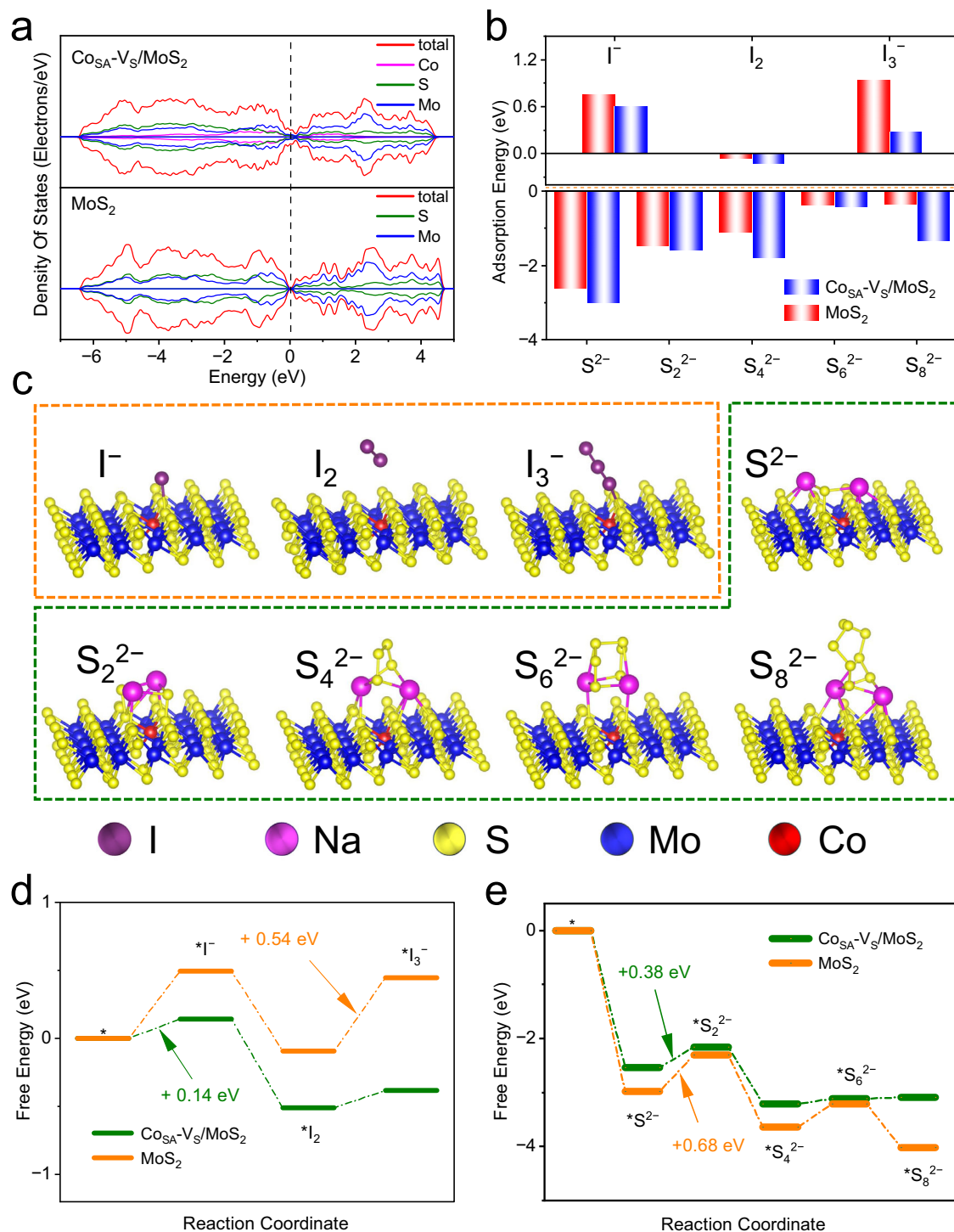
Fig. 4 | Theoretical analyses of Co$_{SA}$-V$_S$/MoS$_2$ and MoS$_2$. a Calculated DOS of Co$_{SA}$-V$_S$/MoS$_2$ and MoS$_2$, with aligned Fermi level. **b** The calculated adsorption energy of I-containing and S-containing species on catalytic surface. **c** The optimized intermediate adsorption configurations for Co$_{SA}$-V$_S$/MoS$_2$. **d, e** Free-energy diagrams of I and S intermediates.

and discharge curves extracted at a current density of 20 mA cm^{-2} with discharge to 50% SOC (Fig. 5d) demonstrate that only a small polarization voltage difference of 113 mV is observed on Co$_{SA}$-V$_S$/MoS$_2$, distinctly lower than those of MoS$_2$ (211 mV) and GF (640 mV). The small overpotential signifies that the water splitting is effectively suppressed to avoid the generation of O$_2$/H$_2$, and the reaction kinetics is greatly accelerated as well[57].

Further, in situ Raman spectrometry was conducted to monitor the S^{2-}/S$_x^{2-}$ and I$^-$/I$_3^-$ conversion on Co$_{SA}$-V$_S$/MoS$_2$ in SIRFB. At the discharging progress, the intensity of S$_2^{2-}$ peak (489 cm^{-1}) reduces while the intensity of S$_4^{2-}$ peak increases accompanied by the peak of S$_4^{2-}$ (193 cm^{-1}) appears[58]; then those (S$_4^{2-}$) peak intensities show opposite trend in the charging progress (Supplementary Fig. 19a, b). Supplementary Fig. 19c, d presents the peak intensity of I$_3^-$ (113 cm^{-1}) reduces in the discharging progress and increases in the charging progress[59]. These findings conform to the in situ UV−vis results.

The EE of Co$_{SA}$-V$_S$/MoS$_2$ derived SIRFB estimated from the first charge and discharge curve is 87.9% (Fig. 5d), larger than those of MoS$_2$
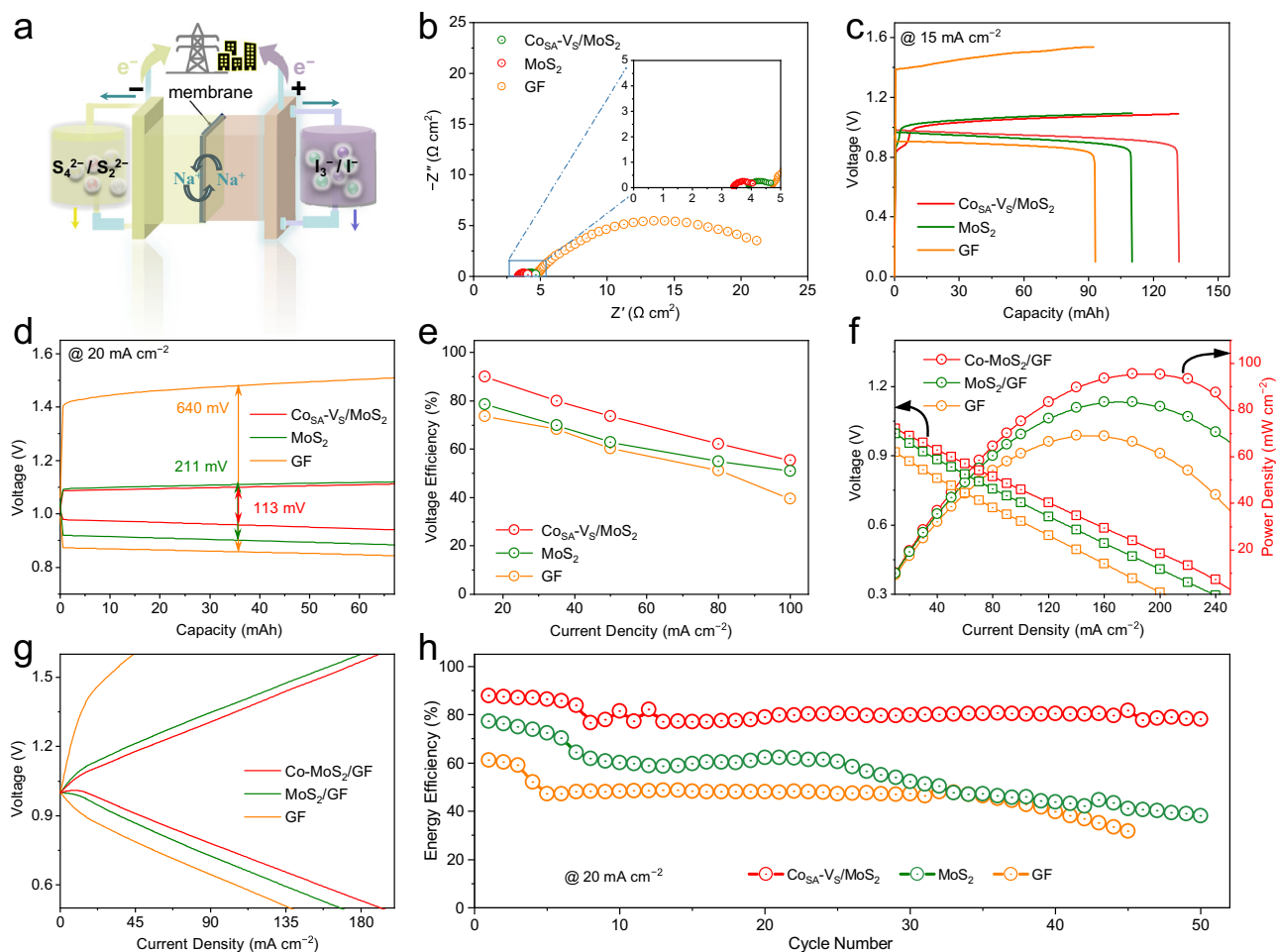
Fig. 5 | Electrochemical performance of aqueous SIRFBs with Co$_{SA}$-V$_S$/MoS$_2$.
a Scheme of the proposed SIRFB configuration. **b** EIS plots of the SIRFBs with GF, MoS$_2$, and Co$_{SA}$-V$_S$/MoS$_2$. **c, d** The first charge and discharge curves recorded at 15 mA cm^{-2} with discharged to 0.1 V (voltage cutoff) or 100% SOC (capacity cutoff) and then charged to 100% SOC (capacity cutoff) and 20 mA cm^{-2} with discharge to 50% SOC, respectively. **e** VE plots at different operational current densities with 50% SOC. **f** Discharge curves and the corresponding power densities with 50% SOC. **g** Charge and discharge polarization curves obtained at different current densities with 50% SOC. **h** The EE taken from galvanostatic cycling test at 20 mA cm^{-2} with 50% SOC.

(77.3%) and GF (61.2%). Further, the voltage efficiency (VE) was calculated according to the equation (VE = EE/CE, CE represents coulombic efficiency) and the results are depicted in Fig. 5e and Supplementary Figs. 20–22. Notably, Co$_{SA}$-V$_S$/MoS$_2$ shows higher VE values over a wide current density range as compared to GF and MoS$_2$ (Fig. 5e), conforming the change trend of CE and EE (Supplementary Figs. 21 and 22). The CE consistently remains approximately 100% at evaluated current densities (Supplementary Fig. 22 and Supplementary Note 5). Meanwhile, the calculated EE of Co$_{SA}$-V$_S$/MoS$_2$ declines from 89.9% at 15 mA cm^{-2} to 55.4% at 100 mA cm^{-2}, attributing to the increased overpotential at larger current densities. The power density of SIRFB with Co$_{SA}$-V$_S$/MoS$_2$ reaches as high as 95.7 mW cm^{-2} (Fig. 5f), outperforming those of GF (69.1 mW cm^{-2}) and MoS$_2$ (83.5 mW cm^{-2}). The open-circuit voltages of the SIRFB with GF, MoS$_2$, and Co$_{SA}$-V$_S$/MoS$_2$ are close to the theoretical value of 1.02 V[12] (Supplementary Fig. 23). In addition, the voltage gap between the charge and discharge curves of the SIRFB with Co$_{SA}$-V$_S$/MoS$_2$ is smaller than those observed in other SIRFBs under the same current density (Fig. 5g), suggesting a better redox reversibility.

Figure 5h illustrates the galvanostatic cycling performance of the SIRFBs operating at 20 mA cm^{-2} with 50% SOC, which confirms that Co$_{SA}$-V$_S$/MoS$_2$ possesses higher EEs relative to others at series of current densities, originating from the reduced charge/discharge overpotentials (Supplementary Fig. 24). Importantly, the SIRFB using Co$_{SA}$-V$_S$/MoS$_2$ achieves an EE of 78.0% at 20 mA cm^{-2} after 50 cycles, corresponding to

88.7% retention. At the same cases, the observed EE and retention for GF and MoS$_2$ are 61.3% and 77.3%, 51.7% and 49.4%, respectively, both of them are inferior to Co$_{SA}$-V$_S$/MoS$_2$. Similarly, the VE and CE of Co$_{SA}$-V$_S$/MoS$_2$ are above 78.6% and 89.6% after 50 cycles at 20 and 30 mA cm^{-2} (Supplementary Figs. 25 and 26). Especially, the average EE of Co$_{SA}$-V$_S$/MoS$_2$ reaches 76.5% at a high current density of 30 mA cm^{-2}, higher than those of Cu$_7$S$_4$/CNT[16] and NiCo$_2$S$_4$[17]. Additionally, the EE retention is 87.1% at 30 mA cm^{-2} after 50 cycles (Supplementary Fig. 26).

To evaluate the durability of Co$_{SA}$-V$_S$/MoS$_2$ after the galvanostatic cycling test, the I-side electrodes were examined (Supplementary Fig. 27), and the results reveal that yellow substance is clearly observed on GF and MoS$_2$. By contrast, there is no I$_2$ residue exist on the surface of Co$_{SA}$-V$_S$/MoS$_2$, corroborating that Co$_{SA}$-V$_S$/MoS$_2$ exhibits better activity towards I$^-$/I$_3^-$ transformation and thus inhibits the I$_2$ production. The Co content in sample Co$_{SA}$-V$_S$/MoS$_2$ is determined to be 1.62 wt% according to the inductively coupled plasma atomic emission spectrometry (ICP-OES); while the Co content is found to be 1.59 wt% after 50 cycles at 20 mA cm^{-2} with the 50% SOC, indicating that scarcely any Co is dissolved during the cycling test. Additional SEM images and XPS analyses of Co$_{SA}$-V$_S$/MoS$_2$ after 50 cycles show a tiny variation for both negative electrode and positive electrode, indicative of its high structural and chemical stability (Supplementary Figs. 28, 29 and Supplementary Note 6). Moreover, the SIRFB using Co$_{SA}$-V$_S$/MoS$_2$ can work stably exceed 850 cycles with an EE retention of 62.0% at a

10 mA cm^{-2} charge/discharge current density with 10% SOC (Supplementary Fig. 30 and Supplementary Note 7), which is greater than those of GF and MoS$_2$. Meanwhile, the initial improved performance of GF is due to the increased roughness and active sites during charge/discharge processes (Supplementary Fig. 31 and Supplementary Note 8), while the activity decay occurred because of the precipitation of I$_2$, enveloping GF and further reduced the reaction area of the electrode[60]. In addition, Co$_{SA}$-V$_S$/MoS$_2$ gives an EE of 93.1% when operates at 10 mA cm^{-2}, which is superior to the recently best-reported results (Supplementary Table 1). The EE values of the SIRFB based on Co$_{SA}$-V$_S$/MoS$_2$ electrode with increasing current densities (from 10 to 100 mA cm^{-2}) at the 50% SOC are fall between 56 and 93% (Supplementary Fig. 32). Overall, the SIRFB with Co$_{SA}$-V$_S$/MoS$_2$ shows competitive advantage in terms of power density, EE, CE, and VE as compared with those of other metal sulfides[12–14] used in SIRFBs (Supplementary Fig. 33 and Supplementary Table 1). Meanwhile, this obtained SIRFB with Co$_{SA}$-V$_S$/MoS$_2$ also show competitive advantages as compared to the vanadium/zinc-bromine redox batteries[61,62].

Besides, we prepared defective MoS$_2$ (H-V$_S$/MoS$_2$, annealed in H$_2$ atmosphere) to assess the synergistic effect of Co$_{SA}$ sites and abundant V$_S$ (Supplementary Fig. 34 and Supplementary Note 9). As expected, the performance of SIRFB with H-V$_S$/MoS$_2$ falls between that of MoS$_2$ and Co$_{SA}$-V$_S$/MoS$_2$, strongly confirming that the combination of Co$_{SA}$ sites and abundant V$_S$ contributes SIRFB enhancement (Supplementary Fig. 35, Supplementary Table 9 and Supplementary Note 10). These findings further emphasize the vital role of single-atom doping in governing the S^{2-}/S$_x^{2-}$ and I$^-$/I$_3^-$ redox kinetic performance.

Discussion

In this study, we fabricated the self-supporting Co$_{SA}$-V$_S$/MoS$_2$ nanosheets on GF substrate by introducing Co$_{SA}$ sites into MoS$_2$ lattice, associating with the formation of V$_S$ and triggering metallic 1T phase transformation. The SIRFB employing Co$_{SA}$-V$_S$/MoS$_2$ demonstrates an EE and a low overpotential of 87.9% and 113 mV at 20 mA cm^{-2}, respectively, accompanying with EE retention remains stable above 88.7% after 50 cycles. Moreover, the SIRFB delivers a power density of 95.7 mW cm^{-2} along with a long operational life of approximately 850 cycles at 10 mA cm^{-2} with 10% SOC. The in situ Raman, in situ UV–vis experiments and DFT calculations indicate that Co$_{SA}$-V$_S$/MoS$_2$ memorably enhances the electrocatalytic activities toward the S^{2-}/S$_x^{2-}$ and I$^-$/I$_3^-$ redox reactions by optimizing the adsorption behaviors of intermediates and reducing the energy barriers. This work presents ingenious and resultful tools to explore high performance single-atom doped MoS$_2$ for sundry advanced SIRFBs application, and more memorably, gains insights into the polysulfide/iodide chemistries.

Methods

Materials

Cobalt nitrate (Co(NO$_3$)$_2$ • 6H$_2$O, > 99.5%) and sodium sulfide nonahydrate (Na$_2$S • 9H$_2$O, 98%) were received from Aladdin. Thiourea (CH$_4$N$_2$S, ≥99.0%), ammonium molybdate ((NH$_4$)$_6$Mo$_7$O$_{24}$ • 4H$_2$O, ≥99.0%), sodium iodide (NaI, 99.5%), sodium chloride (NaCl, ≥99.5%), sublimed sulfur (S, AR), and sulfuric acid (H$_2$SO$_4$, 95.0 ~ 98.0%) were purchased from Sinopharm Chemical Reagent Co., Ltd. Iodine (I$_2$, 99.8%) was purchased from Shanghai Titan Scientific Co., Ltd. The Nafion membrane (SEN-G115 (thickness: 127 μm) was used in S side and the Nafion membrane SEN-K117 (thickness: 175 μm)) was used in I side, both of them were obtained from Suzhou Sinero Technology Co., Ltd., and their lateral dimension is 10*10 cm. GF was from Beijing Jinglong Carbon Technology Co., Ltd. The stoichiometric ratios of S and Na$_2$S were mixed at 25 ± 2 °C to yield sodium polysulfide (Na$_2$S$_x$) electrolytes. Likewise, sodium triiodide (NaI$_3$) electrolytes were obtained according to the addition of stoichiometric ratios of NaI and I$_2$ at 25 ± 2 °C.

Synthesis of electrode materials

The preparation of the Co$_{SA}$-V$_S$/MoS$_2$ involved the initial treatment of the commercially obtained GF, which had immersed in 6 M H$_2$SO$_4$ for approximately 12 h, followed by thorough washing with deionized (DI) water until the flushing water reached a near-neutral (pH ≈ 7). Subsequently, the treated GF was heat treated (300 °C, 2 h). The Co$_{SA}$-V$_S$/MoS$_2$ was synthesized using an in situ one-step hydrothermal method. In this procedure, a mixture containing 0.1765 g of (NH$_4$)$_6$Mo$_7$O$_{24}$ • 4H$_2$O, 0.228 g of CH$_4$N$_2$S, and 0.0291 g of Co(NO$_3$)$_2$ • 6H$_2$O dissolved in 35 mL of DI water was uniformly dispersed. The resultant mixture was transferred to a 50-mL Teflon-lined stainless-steel reactor, where the GF (1.3 cm × 1.3 cm × 3.0 mm) was immersed in the precursor solution. The hydrothermal treatment was performed at 200 °C for 20 h, yielding a black product. Afterward, the product was washed with DI water and freeze dried for 24 h, and then it was annealed at 400 °C for 2 h under a nitrogen (N$_2$) atmosphere. Subsequently, the Co$_{SA}$-V$_S$/MoS$_2$-loaded GF underwent ultrasonic cleaning with water until no discernible Co$_{SA}$-V$_S$/MoS$_2$ particles were observed in the wastewater stream. The final product was then freeze dried for 24 h. The MoS$_2$ electrode was synthesized using a similar approach, except for the addition of a cobalt source.

Electrochemical measurements

CV tests were executed in a three-electrode configuration on a CHI 760E electrochemical workstation with the Ag/AgCl electrode and Pt sheet worked as the reference electrode and the counter electrode, respectively. The working electrodes was established by the catalysts (Co$_{SA}$-V$_S$/MoS$_2$, 10 mg) dispersed in the mixed solution that included 500 μL of DI water, 500 μL of isopropanol, and 20 μL of 5 wt% Nafion, forming a homogeneous ink. Thereafter, 10 μL of the formed ink (catalyst-mixed solution) was loaded on a glassy carbon electrode (diameter of 3 mm), and the electrode was dried at 25 ± 2 °C. The anolyte was 0.02 M S + 0.06 M Na$_2$S + 0.5 M NaCl; the catholyte was 0.1 M NaI$_3$ + 0.5 M NaCl, respectively. The EIS measurement was performed at a frequency range of 0.01 Hz to 1 MHz (5 mV ac oscillation), operate on the open-circuit voltage stable after 60 s, potentiostatic and the number of data points is 12 (per decade of frequency).

Ex situ test

GF, MoS$_2$, and Co$_{SA}$-V$_S$/MoS$_2$ of equivalent mass were soaked in a 5 mL containing iodide or polysulfide aqueous solution with 5.2 mM NaI + 1.3 mM I$_2$ or 12 mM Na$_2$S$_2$ in a side of H-type cells (another side filled in 5 ml DI water), separately, and the admixtures were adequately resting reaction for 12 h to achieve thorough adsorption. The electrolytes were compared and recorded by UV–vis spectra test. The post-electrolysis electrode was washed by DI water and then dried; after that, the electrode was characterized by SEM, XPS and Raman tests. All preparation and testing process under ambient atmosphere at 25 ± 2 °C.

In situ test

The in situ UV–vis spectrometry measurements were conducted using Co$_{SA}$-V$_S$/MoS$_2$ electrode performed in a single cell at a scan rate of 10 mV s^{-1} from 300 to 500 nm (−1.0 V ~ 0.1 V) or from 250 to 400 nm (0.3 V ~ 0.8 V), and the aqueous solution of 0.02 M S + 0.06 M Na$_2$S + 0.5 M NaCl or 0.1 M NaI$_3$ + 0.5 M NaCl, respectively. In situ Raman spectrometry measurements were conducted using Co$_{SA}$-V$_S$/MoS$_2$ electrode performed in SIRFB (at 15 mA cm^{-2} with 100% SOC) from 100 to 600 cm^{-1} or from 70 to 210 cm^{-1}, and the electrolyte volume was 5 mL for anolyte (2.0 M Na$_2$S$_2$) and catholyte (2.0 M NaI + 0.5 M I$_2$), respectively. All preparation and testing process under ambient atmosphere at 25 ± 2 °C.

Assembly of the aqueous SIRFB

This study used the configuration of an aqueous SIRFB (Supplementary Fig. 16). The flow cell pack was procured from Taizhou TiSing Technology Co., Ltd., which resembled previous research reports[3,5,12].

The flow cell featured interdigitated flow fields with a geometric active area of $3.24\,cm^{-2}$ ($1.8\,m \times 1.8\,m$). Commercially available Nafion membranes (G115 and K117) were used as separators. The Nafion membranes were treated with 5% H_2O_2 at 80 °C for 1 h, followed by immersion in 5% H_2SO_4 at 80 °C for an additional 1 h. Subsequently, a 1 M NaOH aqueous solution transformed the H-type (proton conductive) Nafion membranes to Na-type (Na^+ conductive) at 80 °C for 2 h. After each step, the membranes were rinsed with DI water for 30 min to eliminate residual chemicals. GF, MoS_2, and Co_{SA}-V_S/MoS_2 electrodes were used as positive and negative electrodes. The electrolytes were prepared at 25 ± 2 °C under continuous nitrogen gas bubbling for 30 min to prevent oxidation before use. Two half-cell bodies, incorporating the GF, MoS_2, and Co_{SA}-V_S/MoS_2 electrodes as positive and negative electrodes, with the Nafion membrane (G115 and K117) in between, were assembled in ambient air. A peristaltic pump (BT100LC, Baoding Rongbai Precision Pump Manufacturing Co., Ltd.) was used to facilitate the circulation of electrolytes through the flow cell and reservoirs. A silicon tube (with an inner diameter of 3.1 mm) was also used to circulate the electrolyte throughout the system.

Flow cell tests
The SIRFB cells were galvanostatically characterized using a battery testing system (NEWARE, Shenzhen Electronics Co., Ltd). The electrolyte volume was 5 mL for catholyte (2.0 M NaI + 0.5 M I_2) and anolyte (2.0 M Na_2S_2), and controlled the electrolyte flow rate at 10 mL min^{-1} for all experiments. The theoretical capacity is a nominal capacity of 134 mAh, which was calculated by the catholyte (the iodide part, 5 mL of 2.0 M NaI + 0.5 M I_2). The capacity-limiting of the full cell was a controlling factor for charge process, and set up the galvanostatically discharged to 0.1 V (voltage cutoff) or 50% SOC and charged to 50% SOC (capacity cutoff) for the flow cell. Note that the charge process of Fig. 5c was set to 100% SOC (capacity cutoff) after discharged to 0.1 V (voltage cutoff) or 100% SOC (capacity cutoff). In addition, the flow cell was operated at current densities ranging from 10 to 100 mA cm^{-2}. During the cycle test, the N_2 had filled in electrolytes. The extended cycling experiment was conducted at 10, 20, and 30 mA cm^{-2}.

Characterization
XRD patterns were obtained using a Rigaku D/max 2500 diffractometer with Cu Kα radiation ($\lambda = 0.15418$ nm) in the 2θ range of 10°–80° with a scan rate of 10° min^{-1}. Field-emission gun SEM (FEG-SEM) was performed using the Verios 460 L FEI instrument for observation. TEM and mapping images were obtained using an FEI Talos F200X S/TEM with an FEG. X-ray absorption fine structure (XAFS) measurements were performed at Beamline 8-ID, National Synchrotron Light Source II, Brookhaven National Laboratory. Co K-edge absorption spectra were acquired using a cryogenically cooled double crystal Si (1111) monochromator. The spectra were recorded in the fluorescence mode of the monochromator equipped with a passivated implanted planar silicon detector. XPS experiments were performed on a Kratos AXIS Ultra DLD system with Al Kα radiation as the X-ray source. Raman spectroscopy was performed using an HR confocal micro-Raman spectrometer (HORIBA EVOLUTION). The UV–vis absorption spectrum was obtained using a UV-1800PC spectrophotometer (Shanghai Jinghua Technology Instrument Co., Ltd.). The Inductively Coupled Plasma Optical Emission Spectroscopy (ICP-OES) was executed by Thermo Fisher ICPA 6300.

Computational methods
All DFT calculations were performed using the Vienna Ab initio Simulation Package. The Perdew–Burke–Ernzerhof functional with generalized gradient approximation was used to handle the exchange–correlation interactions among electrons. The plane-wave cutoff energy was set to 450 eV, and the convergence criteria for energy and forces were set to 10^{-5} eV and 0.02 eV $Å^{-1}$, respectively.

Surface calculations of Co_{SA}-V_S/MoS_2 (002) and MoS_2 (002) were performed using a $5 \times 5 \times 1$ supercell model, which allowed for the relaxation of all atoms during calculations. A vacuum layer with a thickness of 15 Å in the z-direction was included to prevent interactions among different cells. A $2 \times 2 \times 1$ Monkhorst–Pack k-point grid was also used for the aforementioned structures. In addition, for H_2S, H_2, I_2, and Na_2S molecules, calculations were performed using only the gamma point in a $10 \times 10 \times 10$-Å box. VASPKIT software was utilized for the preprocessing and postprocessing of the computational data.

Data availability
Source data are provided with this paper.

References
1. Chao, D. et al. Roadmap for advanced aqueous batteries: from design of materials to applications. *Sci. Adv.* **6**, eaba4098 (2020).
2. Yang, Z. et al. Alkaline benzoquinone aqueous flow battery for large-scale storage of electrical energy. *Adv. Energy Mater.* **8**, 1702056 (2018).
3. Su, L., Badel, A. F., Cao, C., Hinricher, J. J. & Brushett, F. R. Toward an inexpensive aqueous polysulfide–polyiodide redox flow battery. *Ind. Eng. Chem. Res.* **56**, 9783–9792 (2017).
4. Chen, Q. et al. High-reversibility sulfur anode for advanced aqueous battery. *Adv. Mater.* **36**, 2309038 (2024).
5. Li, Z., Weng, G., Zou, Q., Cong, G. & Lu, Y.-C. A high-energy and low-cost polysulfide/iodide redox flow battery. *Nano Energy* **30**, 283–292 (2016).
6. Zhang, S. et al. Recent progress in polysulfide redox-flow batteries. *Batter. Supercaps* **2**, 627–637 (2019).
7. Lei, J. et al. An active and durable molecular catalyst for aqueous polysulfide-based redox flow batteries. *Nat. Energy* **8**, 1355–1364 (2023).
8. Castañeda, L. F., Walsh, F. C., Nava, J. L. & Ponce de León, C. Graphite felt as a versatile electrode material: properties, reaction environment, performance and applications. *Electrochim. Acta* **258**, 1115–1139 (2017).
9. Liu, W., Lu, W., Zhang, H. & Li, X. Aqueous flow batteries: research and development. *Chem. Eur. J.* **25**, 1649–1664 (2019).
10. Li, Z. & Lu, Y.-C. Material design of aqueous redox flow batteries: fundamental challenges and mitigation strategies. *Adv. Mater.* **32**, 2002132 (2020).
11. Lu, G. et al. Cathode materials for halide-based aqueous redox flow batteries: recent progress and future perspectives. *Nanoscale* **15**, 4250–4260 (2023).
12. Ma, D. et al. Highly active nanostructured CoS_2/CoS heterojunction electrocatalysts for aqueous polysulfide/iodide redox flow batteries. *Nat. Commun.* **10**, 3367 (2019).
13. Zhu, Y. et al. Cu_2CoGeS_4 nanocrystals for high performance aqueous polysulfide/iodide redox flow batteries: enhanced selectively towards the electrocatalytic conversion of polysulfides. *Sustain. Energy Fuels* **4**, 2892–2899 (2020).
14. Zai, J. et al. Sandwiched Cu_7S_4@graphite felt electrode for high performance aqueous polysulfide/iodide redox flow batteries: enhanced cycling stability and electrocatalytic dynamics of polysulfides. *Mater. Chem. Phys.* **250**, 123143 (2020).
15. Gao, M. et al. Successive ionic layer adsorption and reaction–deposited copper sulfide electrocatalyst for high-power polysulfide-based aqueous flow batteries. *Mater. Today Energy* **18**, 100540 (2020).
16. Qin, Y., Li, X., Liu, W. & Lei, X. High-performance aqueous polysulfide-iodide flow battery realized by an efficient bifunctional catalyst based on copper sulfide. *Mater. Today Energy* **21**, 100746 (2021).
17. Liu, J. et al. A highly-stable bifunctional $NiCo_2S_4$ nanoarray@carbon paper electrode for aqueous polysulfide/iodide redox flow battery. *J. Power Sources* **561**, 232607 (2023).

18. Tsega, T. T., Zai, J., Lai, C., Li, X. & Qian, X. Earth-abundant $CuFeS_2$ nanocrystals@graphite felt electrode for high performance aqueous polysulfide/iodide redox flow batteries. *Chin. J. Struct. Chem.* **43**, 100192 (2024).

19. Wang, H.-E. et al. Sulfur-deficient MoS_2 grown inside hollow mesoporous carbon as a functional polysulfide mediator. *J. Mater. Chem. A* **7**, 12068–12074 (2019).

20. Kibsgaard, J., Chen, Z., Reinecke, B. N. & Jaramillo, T. F. Engineering the surface structure of MoS_2 to preferentially expose active edge sites for electrocatalysis. *Nat. Mater.* **11**, 963–969 (2012).

21. Wang, L. et al. The reformation of catalyst: from a trial-and-error synthesis to rational design. *Nano Res.* **17**, 3261–3301 (2024).

22. Liu, F. et al. Phosphorus doping of 3D structural MoS_2 to promote catalytic activity for lithium-sulfur batteries. *Chem. Eng. J.* **431**, 133923 (2022).

23. Liu, J. et al. MoS_2-modified graphite felt as a high performance electrode material for zinc–polyiodide redox flow batteries. *Inorg. Chem. Front.* **6**, 731–735 (2019).

24. Wang, Z. et al. Single-atomic Co-B_2N_2 sites anchored on carbon nanotube arrays promote lithium polysulfide conversion in lithium–sulfur batteries. *Carbon Energy* **5**, e306 (2023).

25. Zhao, S. et al. A universal seeding strategy to synthesize single atom catalysts on 2D materials for electrocatalytic applications. *Adv. Funct. Mater.* **30**, 1906157 (2020).

26. Liu, X. et al. Advances in the synthesis strategies of carbon-based single-atom catalysts and their electrochemical applications. *China Powder Sci. Technol.* **30**, 35–45 (2024).

27. Liang, Z. et al. Co doped MoS_2 as cocatalyst considerably improved photocatalytic hydrogen evolution of g-C_3N_4 in an alkalescent environment. *Chem. Eng. J.* **421**, 130016 (2021).

28. Qin, X., Ke, P., Wang, A. & Kim, K. H. Microstructure, mechanical and tribological behaviors of MoS_2-Ti composite coatings deposited by a hybrid HIPIMS method. *Surf. Coat. Technol.* **228**, 275–281 (2013).

29. Gong, X. et al. Thermally stable hierarchical nanostructures of ultrathin MoS_2 nanosheet-coated CeO_2 hollow spheres as catalyst for ammonia decomposition. *Inorg. Chem.* **55**, 3992–3999 (2016).

30. Yu, Y. et al. High phase-purity 1T'-MoS_2- and 1T'-$MoSe_2$-layered crystals. *Nat. Chem.* **10**, 638–643 (2018).

31. Liu, W. et al. Cobalt-doping of molybdenum disulfide for enhanced catalytic polysulfide conversion in lithium–sulfur batteries. *ACS Nano* **15**, 7491–7499 (2021).

32. Guo, C. et al. Constructing CoO/Co_3S_4 heterostructures embedded in N-doped carbon frameworks for high-performance sodium-ion batteries. *Adv. Funct. Mater.* **29**, 1901925 (2019).

33. Liu, Q. et al. Electron-doped 1T-MoS_2 via interface engineering for enhanced electrocatalytic hydrogen evolution. *Chem. Mater.* **29**, 4738–4744 (2017).

34. Zhang, J. et al. Cobalt-modulated molybdenum–dinitrogen interaction in MoS_2 for catalyzing ammonia synthesis. *J. Am. Chem. Soc.* **141**, 19269–19275 (2019).

35. Wang, T. et al. Multilevel heterostructure of MoS_2/GDYO for lithium-ion batteries. *Adv. Funct. Mater.* **33**, 2308470 (2023).

36. Luo, Z. et al. Chemically activating MoS_2 via spontaneous atomic palladium interfacial doping towards efficient hydrogen evolution. *Nat. Commun.* **9**, 2120 (2018).

37. Li, X. et al. One-step hydrothermal synthesis of high-percentage 1T-phase MoS_2 quantum dots for remarkably enhanced visible-light-driven photocatalytic h_2 evolution. *Appl. Catal. B* **243**, 76–85 (2019).

38. Liu, H.-J., Zhang, S., Chai, Y.-M. & Dong, B. Ligand modulation of active sites to promote cobalt-doped 1T-MoS_2 electrocatalytic hydrogen evolution in alkaline media. *Angew. Chem. Int. Ed.* **62**, e202313845 (2023).

39. Shi, Z. et al. Phase-dependent growth of Pt on MoS_2 for highly efficient H_2 evolution. *Nature* **621**, 300–305 (2023).

40. Gan, T. & Wang, D. Atomically dispersed materials: ideal catalysts in atomic era. *Nano Res.* **17**, 18–38 (2024).

41. Liu, G. et al. MoS_2 monolayer catalyst doped with isolated Co atoms for the hydrodeoxygenation reaction. *Nat. Chem.* **9**, 810–816 (2017).

42. Duan, H. et al. Single-atom-layer catalysis in a MoS_2 monolayer activated by long-range ferromagnetism for the hydrogen evolution reaction: beyond single-atom catalysis. *Angew. Chem. Int. Ed.* **60**, 7251–7258 (2021).

43. Song, H. et al. Cooperative catalytic Mo-S-Co heterojunctions with sulfur vacancies for kinetically boosted lithium-sulfur battery. *Chem. Eng. J.* **450**, 138115 (2022).

44. Tsai, C. et al. Electrochemical generation of sulfur vacancies in the basal plane of MoS_2 for hydrogen evolution. *Nat. Commun.* **8**, 15113 (2017).

45. Huang, S. et al. Synergistically enhanced electrochemical performance of Ni_3S_4–PtX (X = Fe, Ni) heteronanorods as heterogeneous catalysts in dye-sensitized solar cells. *ACS Appl. Mater. Interfaces* **9**, 27607–27617 (2017).

46. Zou, Q. et al. Cation-directed selective polysulfide stabilization in alkali metal–sulfur batteries. *J. Am. Chem. Soc.* **140**, 10740–10748 (2018).

47. Zou, Q. & Lu, Y.-C. Solvent-dictated lithium sulfur redox reactions: an operando UV–vis spectroscopic study. *J. Phys. Chem. Lett.* **7**, 1518–1525 (2016).

48. Yan, W. et al. A tripartite synergistic optimization strategy for zinc-iodine batteries. *Nat. Commun.* **15**, 9702 (2024).

49. Zhang, S.-J. et al. Polyiodide confinement by starch enables shuttle-free Zn–iodine batteries. *Adv. Mater.* **34**, 2201716 (2022).

50. Wang, Y., Li, S. & Yi, J. Electronic and magnetic properties of Co doped MoS_2 monolayer. *Sci. Rep.* **6**, 24153 (2016).

51. Yang, M., Ren, X., Hu, L., Guo, W. & Zhan, J. Facet-controlled activation of persulfate by goethite for tetracycline degradation in aqueous solution. *Chem. Eng. J.* **412**, 128628 (2021).

52. Ning, S. et al. Co^0–$Co^{\delta+}$ interface double-site-mediated C–C coupling for the photothermal conversion of CO_2 into light olefins. *Angew. Chem. Int. Ed.* **62**, e202302253 (2023).

53. Liu, Z. et al. Cobalt-doped molybdenum disulfide for efficient sulfite activation to remove as(iii): preparation, efficacy, and mechanisms. *J. Hazard. Mater.* **452**, 131311 (2023).

54. Li, Q. et al. Forming atom–vacancy interface on the MoS_2 catalyst for efficient hydrodeoxygenation reactions. *Small Methods* **3**, 1800315 (2019).

55. Wu, H. et al. Dual-single-atoms of Pt–Co boost sulfur redox kinetics for ultrafast Li–S batteries. *Carbon Energy* **6**, e422 (2023).

56. Li, Z. & Lu, Y.-C. Polysulfide-based redox flow batteries with long life and low levelized cost enabled by charge-reinforced ion-selective membranes. *Nat. Energy* **6**, 517–528 (2021).

57. Wang, J. et al. Ambient ammonia synthesis via palladium-catalyzed electrohydrogenation of dinitrogen at low overpotential. *Nat. Commun.* **9**, 1795 (2018).

58. Xue, L. et al. In situ/operando Raman techniques in lithium–sulfur batteries. *Small Struct.* **3**, 2100170 (2022).

59. Ma, L. et al. Long-lasting zinc–iodine batteries with ultrahigh areal capacity and boosted rate capability enabled by nickel single-atom electrocatalysts. *Nano Lett.* **23**, 5272–5280 (2023).

60. Dan, X. et al. Rare earth doped CeO_2 uniformly enwraps graphite felt as high current density electrode for all vanadium redox flow battery. *J. Power Sources* **628**, 235921 (2025).

61. Li, Z. et al. Air-breathing aqueous sulfur flow battery for ultralow-cost long-duration electrical storage. *Joule* **1**, 306–327 (2017).

62. Tang, L., Li, T., Lu, W. & Li, X. Lamella-like electrode with high Br_2-entrapping capability and activity enabled by adsorption and spatial confinement effects for bromine-based flow battery. *Sci. Bull.* **67**, 1362–1371 (2022).

Author contributions

Z. Wang and G. Lu synthesized, characterized and performed electrochemical tests. Z. Wang and G. Lu wrote the manuscript with support from all authors. T. Wei and H. Cai co-performed the DFT calculations. G. Meng, Y. Feng, and X. Liu co-edited the paper, to which J. Luo and G. Hu contributed. J. Luo and G. Hu helped with data analysis. G. Meng, K. Chu, D. Wang and X. Liu supervised this work and revised the manuscript. All authors discussed the results and commented on the manuscript.

Competing interests

The authors declare no competing interests.

Additional information

Supplementary information The online version contains supplementary material available at https://doi.org/10.1038/s41467-025-58273-9.

Correspondence and requests for materials should be addressed to Ge Meng, Ke Chu, Dingsheng Wang or Xijun Liu.

Peer review information *Nature Communications* thanks Jiantao Zai, and the other, anonymous, reviewer(s) for their contribution to the peer review of this work. A peer review file is available.

Reprints and permissions information is available at http://www.nature.com/reprints

Publisher's note Springer Nature remains neutral with regard to jurisdictional claims in published maps and institutional affiliations.